How to cite: *Angew. Chem. Int. Ed.* **2025**, e202508419
doi.org/10.1002/anie.202508419

Metal–Organic Frameworks **Very Important Paper**

Engineering the Microporous Environment of Flexible Metal–Organic Frameworks with Bifunctionality for Promoting the Separation of Ethylene from a Ternary Mixture

Kang Wang, Yao Jiang, Hui Zhang, Shaojun Jia, Qi Wang, Peng Cui,* Thamraa AlShahrani, and Shengqian Ma**

Abstract: The separation of ethylene (C_2H_4) from mixtures with carbon dioxide (CO_2) and acetylene (C_2H_2) is of great industrial importance but remains a critical challenge. Here, we report that a rationally designed flexible metal–organic framework (FMOF), featuring a specifically engineered microporous environment with bifunctionality, can promote the efficient one-step separation of C_2H_4 from a ternary mixture. Adsorption isotherms and dynamic breakthrough tests provide experimental evidence confirming the selective adsorption of CO_2 and C_2H_2 over C_2H_4 on such a FMOF, as well as its ability to separate C_2H_4 from a $CO_2/C_2H_2/C_2H_4$ ternary mixture. Theoretical calculations and simulations provide critical insights into the flexible adsorption process and the separation mechanism of the FMOF. The bifunctionality incorporated in FMOF provides exceptionally strong binding of CO_2 and C_2H_2 but inhibition of C_2H_4, which, in turn, enables high adsorption selectivity for CO_2/C_2H_4 and C_2H_2/C_2H_4. This FMOF has high potential for industrial applications in the separation of C_2H_4 from gas mixtures.

Introduction

Ethylene (C_2H_4), one of the largest chemical products globally, serves as the cornerstone of the petrochemical industry.[1–4] The primary industrial technologies for producing C_2H_4 currently include steam cracking and methane oxidative coupling.[5–8] Despite their efficiency, these processes inadvertently yield small amounts of acetylene (C_2H_2) and carbon dioxide (CO_2), which can compromise the downstream catalytic conversion of C_2H_4 to polyethylene by acting as catalyst poisons.[9–11] Consequently, the selective removal of C_2H_2 and CO_2 impurities is essential for the recovery of polymer-grade C_2H_4 from a ternary mixture of $CO_2/C_2H_2/C_2H_4$.[12–14] Because of their similar physical properties, the separation of CO_2, C_2H_2, and C_2H_4 remains a challenging task.[15–17] Industrial separation and purification techniques often rely on multiphase processes using noble metal-catalyzed hydrogenation and organic amine absorption to eliminate the byproducts.[18,19] However, these processes are inherently intricate, energy-intensive, and carry significant environmental drawbacks.[20,21] There is, therefore, an urgent need to develop an alternative technology that is both economically viable and environmentally benign, capable of effectively removing C_2H_2 and CO_2 to produce high-purity C_2H_4 from ternary gas mixtures.

Adsorption separation using porous solid adsorbents has emerged in recent decades as a promising and energy-efficient technology for gas separation and purification.[22–25] The development of high-performance adsorbents is critical to the efficiency of adsorption and separation processes.[26–29] Despite the widespread application of conventional adsorbents such as activated carbons and zeolites, they exhibit certain limitations in terms of adsorption capacity and selectivity.[30–32] Metal–organic frameworks (MOFs) have received significant attention in recent years as a pioneering class of porous materials owing to their highly tunable pore structures, making them ideal materials for gas separation applications.[33–35] Yang et al.[36] conducted a comprehensive review and evaluation of innovative design strategies and separation mechanisms for MOFs, with a focus on addressing multicomponent separation challenges. Their analysis highlighted several powerful strategies, including incorporating adaptive binding sites, integrating multiple binding domains, and exploiting the gate-opening effect. However, very few MOFs have demonstrated the ability to separate C_2H_4 from $CO_2/C_2H_2/C_2H_4$ ternary mixtures in a one-step process, often limited by their unsatisfied working capacity and

[*] K. Wang, Prof. Y. Jiang, S. Jia, Prof. Q. Wang, Prof. P. Cui
School of Chemistry and Chemical Engineering, Hefei University of Technology, Hefei 230009, China
E-mail: yjiang@hfut.edu.cn
cuipeng@hfut.edu.cn

H. Zhang
State Key Laboratory of Advanced Papermaking and Paper-based Materials, School of Light Industry and Engineering, South China University of Technology, Guangzhou 510640, China

Prof. S. Ma
Department of Chemistry, University of North Texas, Denton 76201, USA
E-mail: shengqian.ma@unt.edu

Prof. T. AlShahrani
Department of Physics, College of Science, Princess Nourah bint Abdulrahman University, Riyadh 11564, Saudi Arabia

Additional supporting information can be found online in the Supporting Information section

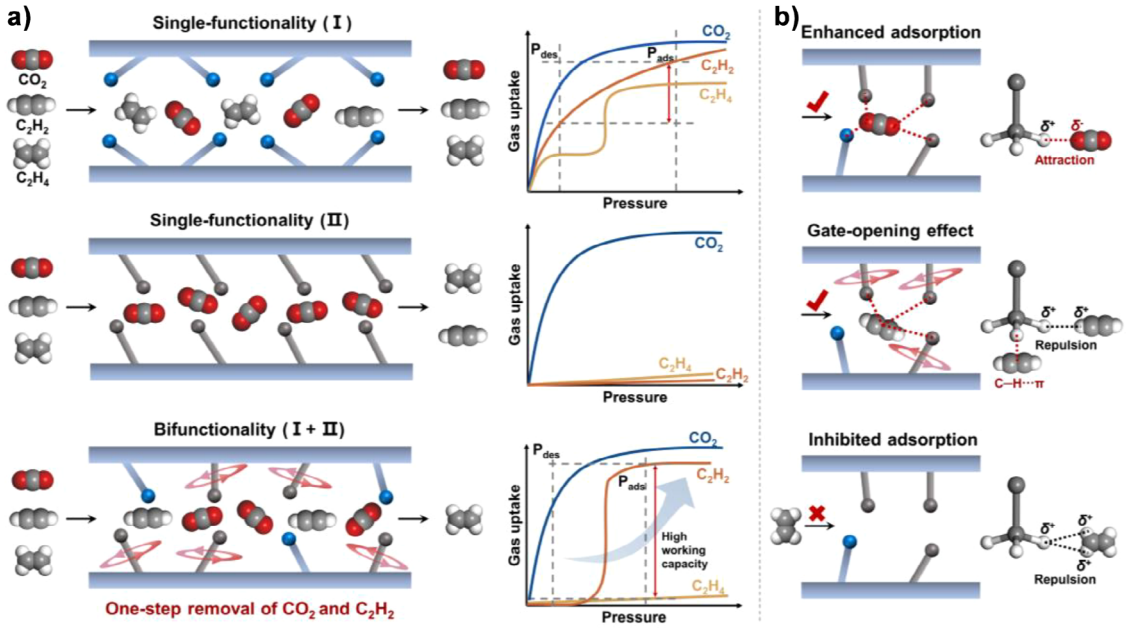

Scheme 1. a) Schematic diagram of the separation of $CO_2/C_2H_2/C_2H_4$ mixture by adsorbents with different functionalities. b) The proposed regulation strategies of the flexible adsorbent with bifunctionality for the binding of CO_2, C_2H_2, and C_2H_4.

selectivity.[37,38] In particular, flexible MOFs (FMOFs) are recognized as intelligent and customizable materials, with reversible structural transformations that can be exploited for enhanced gas storage and separation.[39,40] However, the complexity of factors that influence their flexibility and dynamic behavior complicates the design and regulation of FMOFs compared to the robust counterparts, posing a challenge to their ability to selectively respond to specific guest molecules during practical applications.[41,42] The integration of multifunctionality into porous materials enables for more precise regulation of their pore size, shape, pore environment, and charge characteristics.[43,44] This can generate a diverse range of interactions, thereby facilitating the functionalization of porous materials for selective recognition of guest molecules. In addition, multifunctionality can also induce localized structural distortions or rotational variations, which, in turn, modulate their dynamic structures and adsorption behaviors for guest molecules.[45–47] Consequently, the design of FMOFs with multifunctionality represents a promising strategy for the development of high-performance adsorbents.

Herein, we presented for the first time a rationally designed FMOF, Zn-ox-matz, with bifunctionality to promote the separation of C_2H_4 from a ternary mixture of $CO_2/C_2H_2/C_2H_4$ (Scheme 1). The bifunctionality in Zn-ox-matz was achieved by integrating two triazole-based ligands containing amine and methyl groups. The engineered microporous environment with bifunctionality can enhance the interactions of Zn-ox-matz with specific gas molecules, thereby improving the adsorption working capacity. The incorporation of both methyl and amine groups into Zn-ox-matz provides more binding sites for CO_2 and C_2H_2, while the methyl groups in particular can modulate the dynamic structure and adsorption behavior of Zn-ox-matz toward C_2H_2. In addition, the more compact pore structures and the enhanced positive charge distributions within Zn-ox-matz can increase the electrostatic repulsion interactions with C_2H_4, ultimately promoting the effective one-step removal of C_2H_2 and CO_2 from the ternary mixture of $CO_2/C_2H_2/C_2H_4$. Furthermore, experimental results including adsorption isotherm, ideal adsorption solution theory (IAST) selectivity, adsorption heat, and dynamic breakthrough test confirmed the selective adsorption of CO_2 and C_2H_2 over C_2H_4. Moreover, molecular simulations and density functional theory (DFT) calculations further demonstrated that the multiple adsorption sites and strong binding energies for C_2H_2 and CO_2 on Zn-ox-matz contribute to the efficient separation of C_2H_4 from the ternary mixture of $CO_2/C_2H_2/C_2H_4$. Overall, such a rationally designed FMOF is expected to be a highly promising material for the one-step separation of C_2H_4 from ternary gas mixtures.

Results and Discussion

The samples were prepared through a solvothermal reaction between $ZnCO_3$ and the ligands of oxalic acid, 3-amino-1,2,4-triazole, or/and 3-methyl-1,2,4-triazole, yielding Zn-ox-atz, Zn-ox-mtz, and Zn-ox-matz, respectively (Figures 1a and S1). Structurally, these samples comprise a Zn ion layer bridged by triazole units, with pendant $-CH_3$ or/and $-NH_2$ groups. The Zn ion layer is supported by oxalate units arranged in an outward-facing configuration, which contribute to a three-dimensional framework characterized by one-dimensional pore channels. Unlike Zn-ox-atz and Zn-ox-mtz, Zn-ox-matz features both methyl and amine pendant groups within its pore channels, leading to the formation of two discernible pore sizes with dimensions of 5.2 × 3.4 and 5.0 × 4.2 $Å^2$ (Figure 1b). The proton nuclear magnetic resonance (^1H NMR) spectrum of the digested Zn-ox-matz revealed an

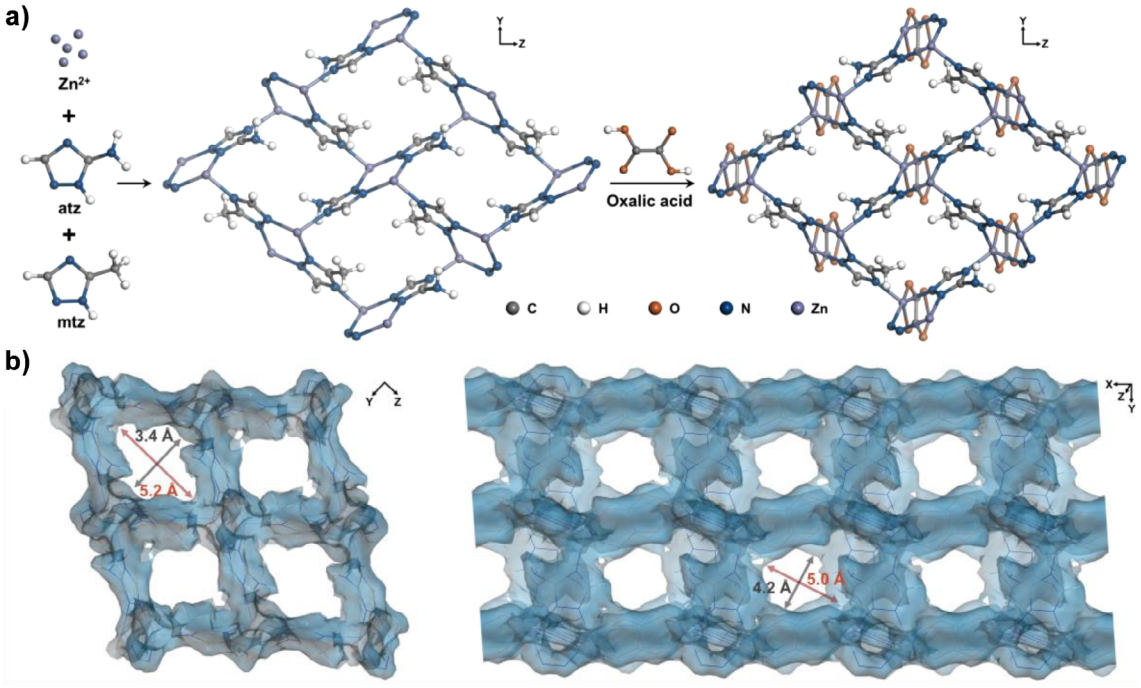

Figure 1. a) Schematic illustration of the assembly of Zn-ox-matz. b) Channel and void surface of Zn-ox-matz.

approximate 1:1 ratio of methyl to amine functional groups (Figure S2). The bulk-phase purity of the synthesized samples was characterized using powder X-ray diffraction (PXRD) technology. As depicted in Figure 2a, the experimental PXRD patterns exhibited excellent agreement with the simulated pattern, thereby confirming the high phase purity of the prepared samples. In addition, thermogravimetric analysis (TGA) and derivative thermogravimetric analysis (DTG) revealed that the Zn-ox-matz remained at temperatures up to 340 °C, which indicates its superior thermal stability (Figure S3).

The infrared (IR) spectrum of Zn-ox-atz illustrated a characteristic band at 3371 cm^{-1}, which is attributed to the $-NH_2$ group in 3-amino-1,2,4-triazole.[48,49] Notably, the broad bands centered at 2962 cm^{-1} corresponded to the symmetrical and antisymmetric stretching vibrations of the typical C–H bonds, which are associated with the $-CH_3$ groups present in 3-methyl-1,2,4-triazole within Zn-ox-mtz.[50] The presence of these two functional groups in Zn-ox-matz demonstrated the successful synthesis of the sample with its desired bifunctionality (Figure 2b). In addition, elemental mapping conducted via scanning electron microscope (SEM) indicated a homogeneous distribution of C, N, O, and Zn elements across the surface of Zn-ox-matz (Figure S4). To further validate the elemental states of Zn-ox-matz, X-ray photoelectron spectroscopy (XPS) were conducted (Figure S5), and the results were found to be in high agreement with the elemental composition determined by SEM-based elemental mapping and energy-dispersive X-ray spectroscopy (EDS) (Figure S6).

To analyze the porous structure of the synthesized samples, nitrogen (N_2) adsorption–desorption isotherms were performed at 77 K (Figure 2c). The isotherms revealed that all the samples exhibited minimal N_2 adsorption capacity, suggesting that N_2 molecules are unable to diffuse into their channels, which is characteristic of porous materials with ultramicropores. To provide a more comprehensive characterization of the pore structure in the different samples, CO_2 adsorption–desorption experiments were carried out at 195 K. Accordingly, the Brunauer–Emmett–Teller (BET) specific surface areas of Zn-ox-atz, Zn-ox-mtz, and Zn-ox-matz were calculated to be 481, 364, and 439 $m^2 \cdot g^{-1}$, respectively. Additionally, a nonlocal density functional theory (NLDFT) model was utilized to predict the pore size distributions of different samples. As illustrated in Figure 2d, Zn-ox-matz exhibited two prominent pore sizes centered at 3.9 and 4.1 Å, which was less than that of Zn-ox-atz and Zn-ox-mtz. Additionally, the pore volumes of Zn-ox-atz, Zn-ox-mtz, and Zn-ox-matz were calculated to be 0.239, 0.220, and 0.235 $cm^3 \cdot g^{-1}$. In comparison to Zn-ox-atz and Zn-ox-trz, the decrease in specific surface area, pore volume, and pore size of Zn-ox-matz can be attributed to the successful incorporation of both methyl and amine groups into the framework, leading to the occupation of certain internal spaces within the pores.

It is clear that CO_2, C_2H_2, and C_2H_4 have similar physical parameters (Table S1). Accordingly, the adsorption–desorption isotherms of CO_2, C_2H_2, and C_2H_4 were tested to evaluate the gas separation performance of different samples (Figures 3, S7 and S8). The Zn-ox-atz demonstrates a high adsorption capacity for CO_2, exhibiting a markedly steeper increase in adsorption in the low-pressure region (Figure 3a), with the adsorption capacity of 86 $cm^3 \cdot g^{-1}$. In contrast, it displays a pronounced hysteresis loop in the stepwise adsorption behavior for C_2H_2 and C_2H_4, indicating its flexible framework structure. Under similar conditions, Zn-ox-mtz exhibited a strong affinity for CO_2, with an adsorption capacity of 70 $cm^3 \cdot g^{-1}$ (Figure 3b). In contrast, the

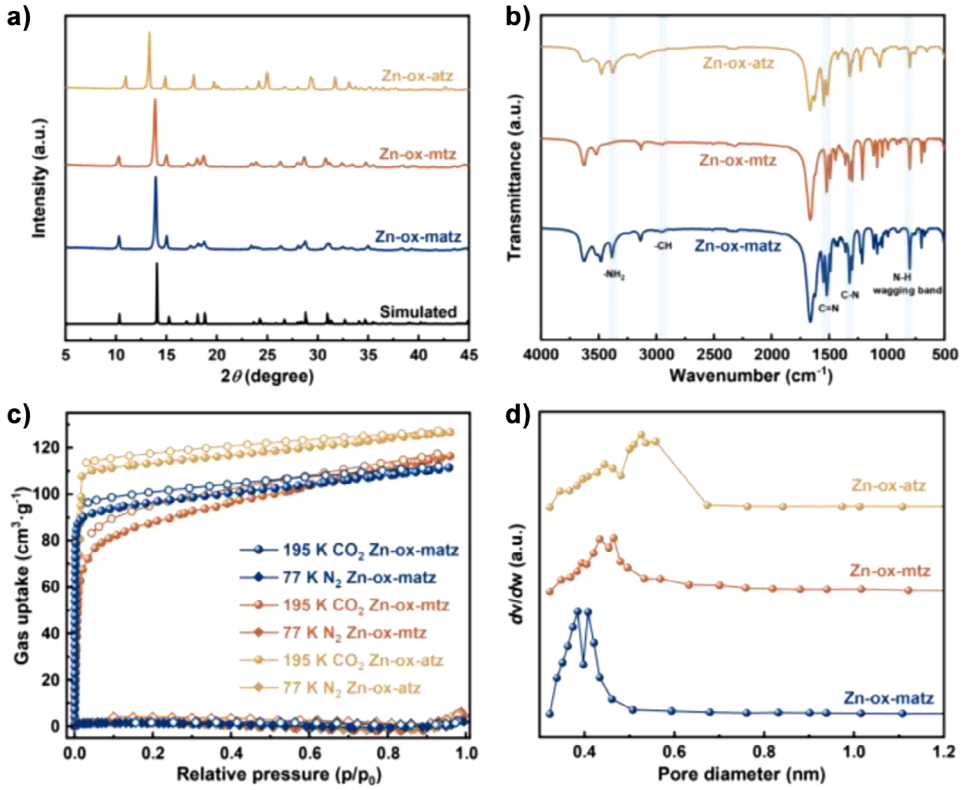

Figure 2. a) PXRD patterns, b) IR spectra, c) N_2 and CO_2 adsorption–desorption isotherms, and d) pore size distributions of different samples.

adsorption capacities for C_2H_2 and C_2H_4 were significantly lower (8 and 10 $cm^3 \cdot g^{-1}$). As illustrated in Figure 3c, the CO_2 adsorption capacity of Zn-ox-matz (84 $cm^3 \cdot g^{-1}$) was significantly greater than that of C_2H_2 (68 $cm^3 \cdot g^{-1}$) and C_2H_4 (8 $cm^3 \cdot g^{-1}$) at 298 K and 1 bar, respectively. Notably, the CO_2 adsorption on Zn-ox-matz exhibited a more rapid increase in the low-pressure region compared to C_2H_2 and C_2H_4, and a significantly higher adsorption capacity for CO_2 (50 $cm^3 \cdot g^{-1}$) compared to C_2H_2 (4 $cm^3 \cdot g^{-1}$) and C_2H_4 (1 $cm^3 \cdot g^{-1}$) at 0.1 bar, indicating a stronger affinity of Zn-ox-matz for CO_2 than C_2H_2 and C_2H_4. However, the incorporation of bifunctionality can eliminate the flexible adsorption behavior of C_2H_4 from Zn-ox-atz to Zn-ox-matz. Also, the adsorption isotherm of C_2H_2 changes from a stepwise adsorption behavior to an *S*-shaped isotherm due to the interactions between gas molecules and Zn-ox-matz with bifunctionality. The presence of amine groups ensures a high adsorption capacity for CO_2, while the methyl groups inhibit the C_2H_4 adsorption and modulates the opening pressure of C_2H_2. As a result, the disparity in adsorption capacity between C_2H_2 and C_2H_4 reached a maximum. Consequently, these results highlight the potential separation of C_2H_4 from a ternary mixture of $CO_2/C_2H_2/C_2H_4$. Also, the adsorption separation performance of a physically mixed sample of Zn-ox-atz and Zn-ox-mtz was evaluated (Figure S9). The results indicated that the adsorption capacity for C_2H_2 and C_2H_4 was improved, while the adsorption selectivities for CO_2/C_2H_4 and C_2H_2/C_2H_4 were notably lower compared than for Zn-ox-matz.

To further evaluate the separation performance of Zn-ox-matz for gas mixtures, IAST selectivity calculations were performed by fitting the adsorption isotherms to the dual-site Langmuir–Freundlich (DSLF) model (Figures S10–S13, Table S5). The results showed that Zn-ox-amtz exhibited a C_2H_2/C_2H_4 selectivity of 4.2 and a CO_2/C_2H_4 selectivity of 1293.7 (Figure 3d), which significantly suppressed many previously reported values (Figure 3e,f, Tables S2–S4). In addition, the separation potential ($\Delta q = q_1 y_2 / y_1 - q_2$) was employed as a combined selectivity-capacity metric to provide a deeper evaluation of the separation performance of Zn-ox-matz. The results indicated that the separation potential of CO_2/C_2H_4 and C_2H_2/C_2H_4 can reach 121.4 and 24.89 $mmol \cdot g^{-1}$ at 100 kPa and 298 K (Figures S14 and S15). Furthermore, the isosteric adsorption heat (Q_{st}) often provides valuable insight into the binding affinity between the adsorbent and adsorbate. The Q_{st} values of Zn-ox-matz at zero coverage for CO_2 (39.89 $kJ \cdot mol^{-1}$) and C_2H_2 (25.71 $kJ \cdot mol^{-1}$) were found to be higher than that for C_2H_4 (20.81 $kJ \cdot mol^{-1}$) (Figures S16–S18), suggesting a stronger interaction between Zn-ox-matz and CO_2 and C_2H_2 compared to C_2H_4.

Dynamic column breakthrough experiments were performed with mixtures of C_2H_2/C_2H_4, CO_2/C_2H_4, and $CO_2/C_2H_2/C_2H_4$ to further evaluate the potentially practical separation performance of Zn-ox-matz (Figures 3e–g and S19). As shown in Figure 3e, it can be observed that C_2H_4 was eluted first due to the its relatively weak interaction with Zn-ox-matz. In contrast, C_2H_2 was detected after 10 $min \cdot g^{-1}$, indicating the higher adsorption of C_2H_2 than

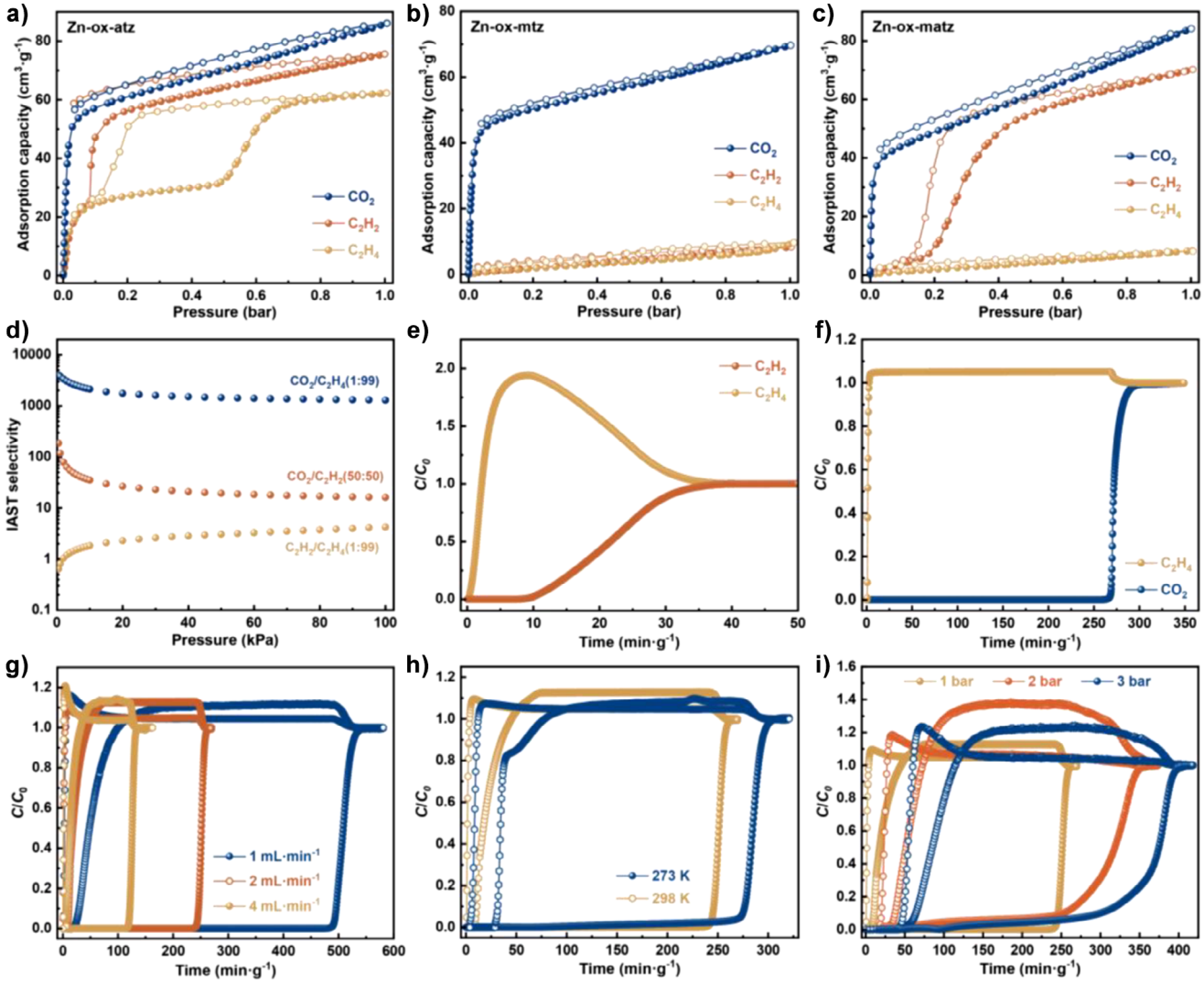

Figure 3. Adsorption isotherms of CO_2, C_2H_2, and C_2H_4 on a) Zn-ox-atz, b) Zn-ox-mtz, and c) Zn-ox-matz at 298 K. d) IAST selectivity of CO_2/C_2H_4, C_2H_2/C_2H_4, and CO_2/C_2H_2 on Zn-ox-matz. Breakthrough curves for the binary mixtures of e) C_2H_2/C_2H_4 (50/50) and f) CO_2/C_2H_4 (1/99) on Zn-ox-matz. Breakthrough curves for the ternary mixture of $CO_2/C_2H_2/C_2H_4$ (1/1/98) under various g) gas flow rates, h) temperatures, and i) pressures on Zn-ox-matz.

that of C_2H_4 on Zn-ox-matz. Similarly, for the mixture of CO_2/C_2H_4 (1/99), CO_2 can be detected until 258.1 min·g^{-1}, indicating a very strong interaction between CO_2 and Zn-ox-matz (Figure 3f). In addition, Zn-ox-matz was applied to a ternary mixture of $CO_2/C_2H_2/C_2H_4$. Figure 3g shows that C_2H_4 was eluted first at 0.62 min·g^{-1}, followed by C_2H_2 at 8.36 min·g^{-1} and CO_2 at 197.51 min·g^{-1}. During this process, Zn-ox-matz can produce high-purity C_2H_4 (99.95%) at a concentration of 1.60 mmol·g^{-1} from a ternary mixture of $CO_2/C_2H_2/C_2H_4$ (1/1/98), which is higher than that reported for some well-known MOFs (Figure S20). Based on breakthrough curves, the dynamic separation selectivities of CO_2/C_2H_4 and C_2H_2/C_2H_4 on Zn-ox-matz were calculated to be 106.91 and 10.88, respectively (Figure S21). To further investigate the dynamic separation efficiency of Zn-ox-matz for a $CO_2/C_2H_2/C_2H_4$ mixture, breakthrough experiments were conducted under varying gas flow rates (Figure 3g) and at different temperatures (Figure 3h). The results consistently demonstrated the high separation efficiency of Zn-ox-matz for this mixture.

Given the structural flexibility of Zn-ox-matz, further breakthrough experiments were carried out at higher pressures to investigate its separation performance for a $CO_2/C_2H_2/C_2H_4$ mixture. As illustrated in Figure 3i, the separation efficiency of Zn-ox-matz exhibited a significantly improvement with increasing pressure. Notably, the retention time of C_2H_2 was extended to 21.1 min·g^{-1} at 2 bar and 31.0 min·g^{-1} at 3 bar, respectively. Correspondingly, the calculated C_2H_4 productivity reached 3.12 mmol·g^{-1} at 2 bar and 6.46 mmol·g^{-1} at 3 bar. These results indicate that the flexibility of Zn-ox-matz can promote the separation of C_2H_4 from a $CO_2/C_2H_2/C_2H_4$ mixture under higher pressure conditions.

To further investigate the reusability of Zn-ox-matz for gas separation applications, cyclic adsorption and breakthrough

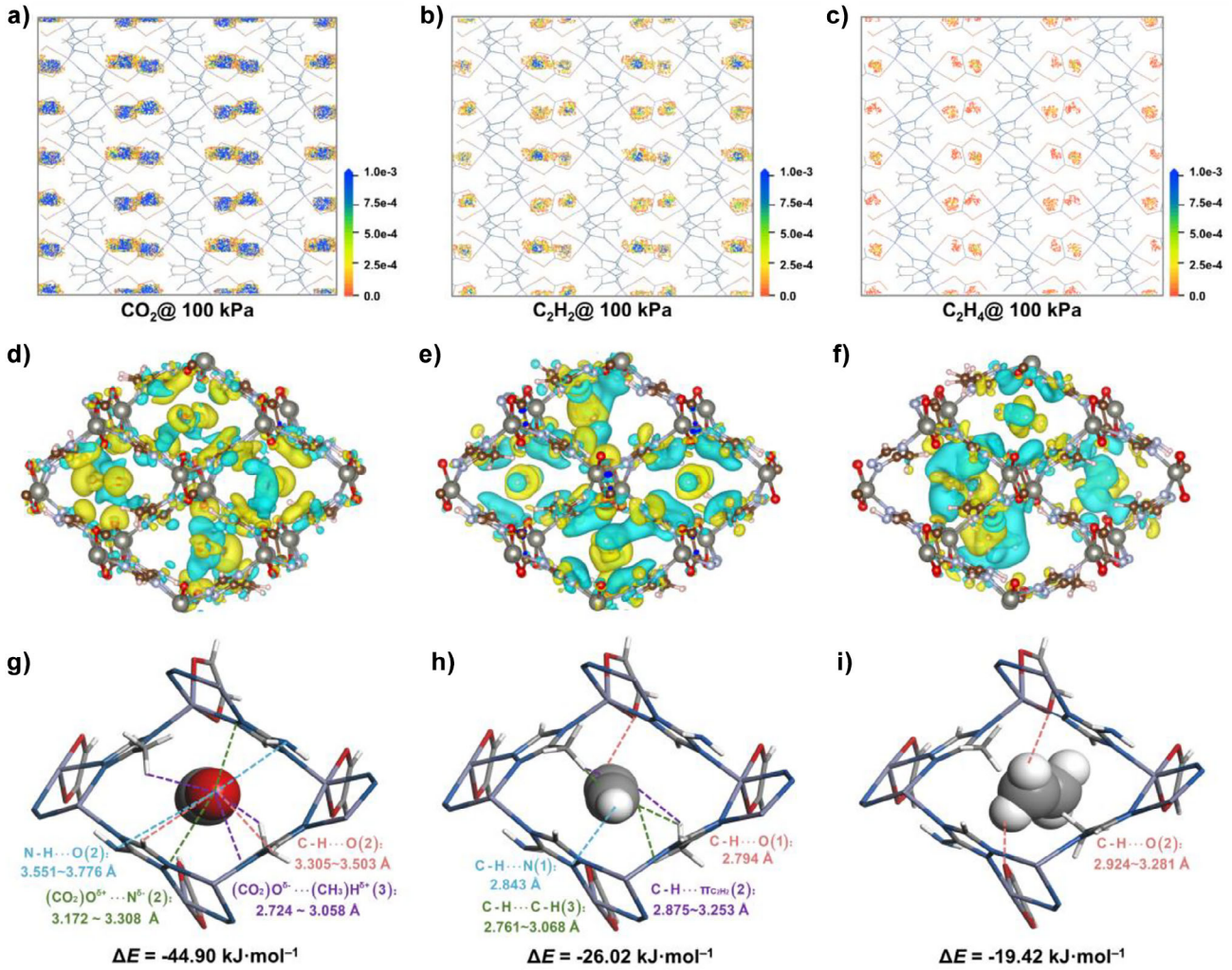

Figure 4. Adsorption density distributions of a) CO_2, b) C_2H_2, and c) C_2H_4 on Zn-ox-matz at 100 kPa. Induced charge densities for d) CO_2, e) C_2H_2, and f) C_2H_4 with an iso-level of 0.001 electrons per $Å^3$. The blue highlights represent the decrease in charge and yellow highlights show the increase in charge after binding of the gas molecules. Calculated preferential binding sites and binding energies of g) CO_2, h) C_2H_2, and i) C_2H_4 on Zn-ox-matz.

experiments were performed for C_2H_2, C_2H_4, and CO_2 (Figures S22 and S23). Remarkably, there was no detectable loss of adsorption capacity for any of these gases, and the cyclic breakthrough curves remained highly consistent throughout the cyclic tests, suggesting the exceptional reusability of Zn-ox-matz for the purification of C_2H_4 from ternary gas mixtures. It also demonstrated excellent stability under different acid/base conditions and various organic solvents from PXRD analysis (Figures S24–S28). The 195 K CO_2 adsorption–desorption curves also confirmed the high stability of Zn-ox-matz under acid condiction (Figure S29). Furthermore, a comparative analysis of breakthrough experiments conducted under both dry and humid conditions (RH = 11.5%) revealed efficient $CO_2/C_2H_2/C_2H_4$ separation from a water vapor mixture on Zn-ox-matz (Figure S30).

Grand Canonical Monte Carlo (GCMC) simulations were carried out to study the preferential interaction regions and the density distributions of CO_2, C_2H_2, and C_2H_4 on Zn-ox-matz (Figures 4a–c and S31). The results indicated that the density distributions of CO_2, C_2H_2, and C_2H_4 on Zn-ox-matz are predominantly concentrated in the symmetrical regions of the rhombic channels, particularly proximal the oxygen atoms of the oxalate. Over the pressure range of 1 to 100 kPa, the adsorption density distributions of CO_2, C_2H_2, and C_2H_4 all increased with increasing pressure. Notably, the adsorption density distributions of CO_2 and C_2H_2 were significantly higher than that of C_2H_4 on Zn-ox-matz, confirming its superior adsorption performance for CO_2 and C_2H_2 compared to C_2H_4. These results are good in agreement with the above experimental adsorption results.

To further elucidate the binding affinity of CO_2, C_2H_2, and C_2H_4 on Zn-ox-matz, the DFT calculated induced charge density and preferential binding sites were performed (Figure 4d-i). The calculated binding energies for CO_2, C_2H_2, and C_2H_4 on Zn-ox-matz were found to be 44.90, 26.02, and 19.42 $kJ·mol^{-1}$, respectively, which are in good agreement with the experimentally predicted isosteric adsorption heats. In addition, induced charge density plots further revealed significant charge transfer during the adsorption process (Figure 4d–f), indicating strong

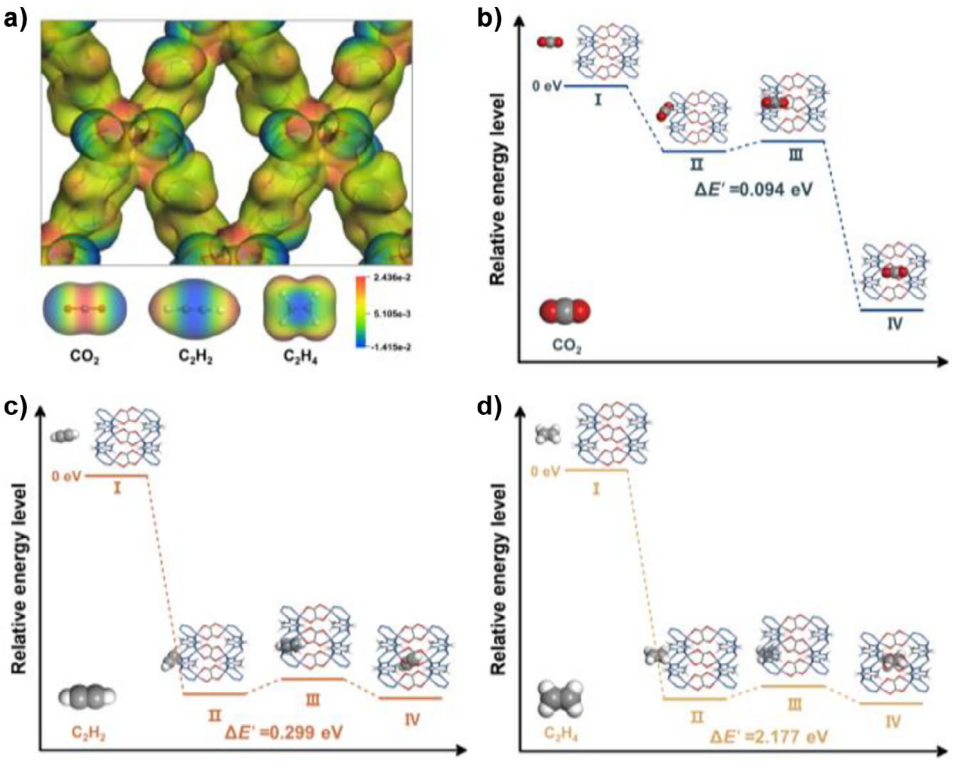

Figure 5. a) ESP maps of Zn-ox-matz and gas molecules. The energy pathways and corresponding energy levels for the adsorption processes of b) CO_2, c) C_2H_2, and d) C_2H_4 into Zn-ox-matz.

interactions between the Zn-ox-matz and CO_2. Specifically, the oxygen atom of CO_2 established strong interactions with two adjacent methyl hydrogen atoms, resulting in a pronounced $(CO_2)O^{\delta-}\cdots(CH_3)H^{\delta+}$ with distances ranging from 2.742 to 3.058 Å (Figure 4g). However, this interaction was insufficient to induce rotation or oscillation of the methyl group. Furthermore, each CO_2 molecule interacted with two triazole ligands, forming two $(CO_2)C^{\delta+}\cdots N^{\delta-}$ interactions with distances ranging from 3.172 to 3.308 Å, and hydrogen bonding with the N─H···O and ─NH_2 functional group with distances ranging from 3.551 to 3.776 Å, as well as interacting with the carbon atom of the triazole to form C─H···O interactions with distances of 3.503 and 3.305 Å. Due to these multiple interactions, CO_2 was tightly captured within the pores of Zn-ox-matz. In addition, the induced charge density result showed that the interaction between C_2H_2 and Zn-ox-matz was primarily through the hydrogen atoms of the methyl groups and the π-electrons of C_2H_2 (Figure 4e), resulting in strong C─H···π_{C2H2} interactions with distances ranging from 2.875 to 3.253 Å (Figure 4h). Simultaneously, strong C─H···C─H interactions with distances ranging from 2.761 to 3.068 Å were observed between the Zn-ox-matz and C_2H_2. C_2H_2 interacted with an oxygen atom of an oxalic acid, forming a C─H···O interaction with a distance of 2.794 Å, and with a nitrogen atom of a triazole, forming a C─H···N interaction with a distance of 2.843 Å. In contrast, each C_2H_4 only interacted with two oxygen atoms of oxalic acid, forming weak C─H···O interactions (H─O, 2.924–3.281 Å) (Figures 4f–i). Consequently, the induced charge density and binding energy analysis results indicated that Zn-ox-matz has stronger interactions with CO_2 and C_2H_2 compared to C_2H_4.

To elucidate the structural changes of Zn-ox-matz, its dynamic behavior was further simulated using Ab initio molecular dynamics.[51] The results revealed that the gate-opening effect arisen from the multiple strong interactions between C_2H_2 and the methyl groups (Supplementary movies 1–3). These interactions can regulate the rotation and torsion of the methyl groups, resulting in the formation of pores that match the shape and size of C_2H_2. This configuration promotes the passage of C_2H_2 molecules and their diffusion into adjacent channels. In contrast, CO_2 and C_2H_4 do not form strong interactions with methyl groups, preventing rotation and resulting in an absence of flexible adsorption behavior.

To gain a deeper understanding of the reduced adsorption capacity of C_2H_4 on Zn-ox-matz, DFT calculated electrostatic potential (ESP) maps of gas molecules and the pore surfaces of Zn-ox-matz were investigated (Figures 5a and S32). Within Zn-ox-matz, positive potentials were predominantly localized around the hydrogen atoms of the ligands and the metal centers, while negative potentials were localized near the oxygen and nitrogen atoms of the ligands. In contrast to Zn-ox-atz, Zn-ox-matz demonstrated a more positively charged pore surface due to the additional hydrogen atoms derived from methyl groups lining the channel pathways. Zn-ox-atz is characterized by a spacious and open pore structure, which allows optimal adsorption configurations for C_2H_2 and CO_2 across various orientations. The introduction of methyl groups leads to a more compact pore structure, with an

increased density of hydrogen atoms along the channels, thereby generating a positively charged pore environment. The pore structure of Zn-ox-matz is well matched to the molecular dimension of CO_2, allowing for multiple non-covalent interactions between CO_2 and the pore surfaces. These interactions can enhance the selective adsorption of CO_2 as the electrostatic potential of CO_2 is complementary to that of the Zn-ox-matz pore surface. However, the polarities of C_2H_2 and C_2H_4 are opposite to that of CO_2, resulting in electrostatic repulsion by the methyl groups in Zn-ox-matz.

To explore the movement process of gas molecules, DFT calculations were conducted to investigate the energy levels associated with the diffusion of CO_2, C_2H_2, and C_2H_4 into Zn-ox-matz (Figure 5b,d). The rate-determining step in these diffusion processes is primarily driven by the maximun energy barrier required in the transition states (TS) from surface adsorption TS(II) to diffusion into the pores TS(III). As shown in Figure 5b, the diffusion barrier for CO_2 within the Zn-ox-matz was calculated to be 0.0944 eV, suggesting facile transport through the pore channels. Because of the improved steric hindrance caused by the bifunctionality, the diffusion barrier for C_2H_2 was increased to 0.299 eV (Figure 5c). Conversely, the diffusion barrier for C_2H_4 was significantly higher at 2.178 eV, indicating hindered diffusion and consequently minimal adsorption capacity for C_2H_4 on Zn-ox-matz.

Conclusion

In summary, this study successfully achieved for the first time a rationally designed FMOF of Zn-ox-matz featuring an engineered microporous environment with bifunctionality for the separation of C_2H_4 from a ternary mixture. The bifunctionality of both methyl and amine groups in Zn-ox-matz can enhance the interactions with CO_2 and C_2H_2, while the methyl groups specifically modulate the dynamic structure and flexible adsorption behavior for C_2H_2, as well as provide electrostatic repulsion against C_2H_4. Comprehensive experimental studies, supported by molecular simulations and DFT calculations, elucidated that the multiple adsorption sites and strong binding energies for CO_2, combined with C_2H_2 adsorption regulated structural flexibility on Zn-ox-matz, contributed to the efficient separation of C_2H_4 from a ternary mixture of $CO_2/C_2H_2/C_2H_4$. Looking forward, the present work paves the way for the development of efficient adsorbents for practical applications in C_2H_4 separation and purification.

Acknowledgements

This work was supported by the National Natural Science Foundation of China (22208078 and 22478092) and the Fundamental Research Funds for the Central Universities (JZ2025HGTG0258). Partial support from the Robert A. Welch Foundation (B-0027) (S. M.) and Princess Nourah bint Abdulrahman University Researchers Supporting Project (PNURSP2025R1), Riyadh, Saudi Arabia (T.A.) is also acknowledged.

Conflict of Interests

The authors declare no conflict of interest.

Data Availability Statement

The data that support the findings of this study are available from the corresponding author upon reasonable request.

Keywords: Adsorption separation · Bifunctionality · Ethylene purification · Flexible metal–organic framework · Pore engineering

[1] Z. Di, C. Liu, J. Pang, S. Zou, Z. Ji, F. Hu, C. Chen, D. Yuan, M. Hong, M. Wu, *Angew. Chem. Int. Ed.* **2022**, *61*, e202210343.
[2] G.-D. Wang, Y.-Z. Li, W.-J. Shi, L. Hou, Y.-Y. Wang, Z. Zhu, *Angew. Chem. Int. Ed.* **2023**, *62*, e202311654.
[3] Z. Xu, X. Xiong, J. Xiong, R. Krishna, L. Li, Y. Fan, F. Luo, B. Chen, *Nat. Commun.* **2020**, *11*, 3163.
[4] R.-B. Lin, H. Wu, L. Li, X.-L. Tang, Z. Li, J. Gao, H. Cui, W. Zhou, B. Chen, *J. Am. Chem. Soc.* **2018**, *140*, 12940–12946;
[5] P.-D. Zhang, X. Zhang, X.-Q. Wu, Z.-C. Xu, J.-R. Li, *AIChE J.* **2022**, *68*, e17752.
[6] S. Ainiwaner, H. Huang, J.-J. Zheng, F. Li, X.-T. Yang, Y.-Y. Guo, F. Yuan, M.-S. Yao, Y. Gu, *Nano Res.* **2024**, *17*, 10083–10087.
[7] C. Hao, Z. Ge, R. Krishna, H. Ren, H. Zhu, Y. Chi, W. Zhao, X. Liu, W. Guo, *Chem. Eng. J.* **2023**, *471*, 144533.
[8] M.-H. Yu, H. Fang, H.-L. Huang, M. Zhao, Z.-Y. Su, H.-X. Nie, Z. Chang, T.-L. Hu, *Small* **2023**, *19*, 2300821.
[9] Y. Duan, Y. Huang, C. Wang, Q. Wang, K. Ge, Z. Lu, H. Wang, J. Duan, J. Bai, W. Jin, *Chem. Sci.* **2023**, *14*, 4605–4611.
[10] G.-D. Wang, Y.-Z. Li, R. Krishna, Z.-Z. Yan, L. Hou, Y.-Y. Wang, Z. Zhu, *Chem. Eng. J.* **2024**, *485*, 149587.
[11] W. Fan, X. Wang, X. Zhang, X. Liu, Y. Wang, Z. Kang, F. Dai, B. Xu, R. Wang, D. Sun, *ACS Cent. Sci.* **2019**, *5*, 1261–1268.
[12] H. Chen, X. Jiang, B. Wang, Y. Ren, B. Zhang, J. Gui, X. Cui, L. Sun, J. Jiang, W. Yan, J. Li, L. Li, *Chem. Eng. Sci.* **2025**, *301*, 120729.
[13] X. Shi, B. Zhang, H. Chen, J. Li, L. Li, *Sep. Purif. Technol.* **2023**, *327*, 124953.
[14] H. Chen, B. Wang, B. Zhang, J. Chen, J. Gui, X. Shi, W. Yan, J. Li, L. Li, *Chem. Sci.* **2023**, *14*, 7068–7075.
[15] Q. Dong, Y. Huang, K. Hyeon-Deuk, I. Y. Chang, J. Wan, C. Chen, J. Duan, W. Jin, S. Kitagawa, *Adv. Funct. Mater.* **2022**, *32*, 2203745.
[16] D. Song, S. Zou, Z. Ji, Y. Li, H. Li, Y. zhou, C. Chen, Q. Chen, M. Wu, *Angew. Chem. Int. Ed.* **2025**, *64*, e202423496.
[17] J.-W. Wang, X.-B. Mu, S.-C. Fan, Y. Xiao, G.-J. Fan, D.-C. Pan, W. Yuan, Q.-G. Zhai, *Inorg. Chem.* **2024**, *63*, 3436–3443.
[18] R.-S. Liu, M. Wang, W.-C. Li, X.-J. Zhang, C.-T. Wang, G.-P. Hao, A.-H. Lu, *Small* **2024**, *20*, 2401965.
[19] J. Luo, G. Yang, G. Zhang, Z. Huang, J. Peng, Y. Luo, X. Wang, C. Yang, J. Jiang, D. Cao, B. Chen, H. Tang, J. Xiao, *Chem* **2024**, *10*, 3148–3158.

[20] M. Shivanna, K.-i. Otake, S. Hiraide, T. Fujikawa, P. Wang, Y. Gu, H. Ashitani, S. Kawaguchi, Y. Kubota, M. T. Miyahara, S. Kitagawa, *Angew. Chem. Int. Ed.* **2023**, *62*, e202308438.
[21] L. Zhang, T. Xiao, X. Zeng, J. You, Z. He, C.-X. Chen, Q. Wang, A. Nafady, A. M. Al-Enizi, S. Ma, *J. Am. Chem. Soc.* **2024**, *146*, 7341–7351.
[22] J.-H. Li, Y.-W. Gan, J.-X. Chen, R.-B. Lin, Y. Yang, H. Wu, W. Zhou, B. Chen, X.-M. Chen, *Angew. Chem. Int. Ed.* **2024**, *63*, e202400823.
[23] H. Xiong, Y. Peng, X. Liu, P. Wang, P. Zhang, L. Yang, J. Liu, H. Shuai, L. Wang, Z. Deng, S. Chen, J. Chen, Z. Zhou, S. Deng, J. Wang, *Adv. Mater.* **2024**, *36*, 2401693.
[24] X. Zhu, T. Ke, J. Zhou, Y. Song, Q. Xu, Z. Zhang, Z. Bao, Y. Yang, Q. Ren, Q. Yang, *J. Am. Chem. Soc.* **2023**, *145*, 9254–9263.
[25] Y.-Y. Xiong, C.-X. Chen, T. Pham, Z.-W. Wei, A. Forrest Katherine, M. Pan, C.-Y. Su, *CCS Chem.* **2023**, *6*, 241–254.
[26] E. Wu, X.-W. Gu, D. Liu, X. Zhang, H. Wu, W. Zhou, G. Qian, B. Li, *Nat. Commun.* **2023**, *14*, 6146.
[27] H. Sun, F. Chen, R. Chen, J. Li, L. Guo, Y. Liu, F. Shen, Q. Yang, Z. Zhang, Q. Ren, Z. Bao, *Small* **2023**, *19*, 2208182.
[28] Z. Zhang, Y. Chen, K. Chai, C. Kang, S. B. Peh, H. Li, J. Ren, X. Shi, X. Han, C. Dejoie, S. J. Day, S. Yang, D. Zhao, *Nat. Commun.* **2023**, *14*, 3789.
[29] X.-P. Fu, Y.-L. Wang, X.-F. Zhang, Z. Zhang, C.-T. He, Q.-Y. Liu, *CCS Chem.* **2022**, *4*, 3416–3425.
[30] H. Chen, B. Wang, B. Zhang, Y. Ren, J. Chen, J. Gui, X. Shi, W. Yan, J. Li, L. Li, *Inorg. Chem. Front.* **2024**, *11*, 2427–2435.
[31] Y. Chen, H. Jiang, Q. Peng, D. Fang, C. Liu, K. Wu, Y. Chen, W. Gao, H. Wang, G. Guo, F. Yang, P. Li, B. Shen, F. Zhang, D. Wu, H. Sun, *Chem. Eng. J.* **2023**, *473*, 145151.
[32] P. Wang, S. Shang, H. Xiong, X. Liu, J. Liu, H. Shuai, L. Wang, Z. Zhu, Z. Zhao, Y. Peng, J. Chen, S. Chen, Z. Zhou, J. Wang, *J. Mater. Chem. A* **2025**, *13*, 1915–1922.
[33] Y. Wang, X. Jia, H. Yang, Y. Wang, X. Chen, A. N. Hong, J. Li, X. Bu, P. Feng, *Angew. Chem. Int. Ed.* **2020**, *59*, 19027–19030.
[34] J. H. Choe, H. Kim, H. Yun, M. Kang, S. Park, S. Yu, C. S. Hong, *J. Am. Chem. Soc.* **2024**, *146*, 646–659.
[35] B. Song, Y. Liang, Y. Zhou, L. Zhang, H. Li, N.-X. Zhu, B. Z. Tang, D. Zhao, B. Liu, *J. Am. Chem. Soc.* **2024**, *146*, 14835–14843.
[36] L.-F. Yang, P.-X. Zhang, J.-Y. Cui, X.-L. Cui, H.-B. Xing, *Angew. Chem. Int. Ed.* **2024**, *63*, e202414503.
[37] R. Yang, T. Zhang, J. Wang, X. Zhang, J.-W. Cao, Y. Wang, K.-J. Chen, *Chem. Biochem. Eng.* **2024**, *2*, 35–40.
[38] Z. Zhao, Y. Liu, X. Liu, Y. Liu, J. Chen, S. Chen, S. Deng, J. Wang, *AIChE J.* **2023**, *69*, e18046.
[39] Z.-J. Lin, J. Lü, M. Hong, R. Cao, *Chem. Soc. Rev.* **2014**, *43*, 5867–5895.
[40] S.-S. Meng, M. Xu, H. Guan, C. Chen, P. Cai, B. Dong, W.-S. Tan, Y.-H. Gu, W.-Q. Tang, L.-G. Xie, S. Yuan, Y. Han, X. Kong, Z.-Y. Gu, *Nat. Commun.* **2023**, *14*, 5347.
[41] H. Wang, M. Warren, J. Jagiello, S. Jensen, S. K. Ghose, K. Tan, L. Yu, T. J. Emge, T. Thonhauser, J. Li, *J. Am. Chem. Soc.* **2020**, *142*, 20088–20097.
[42] X. Wang, R. Krishna, L. Li, B. Wang, T. He, Y.-Z. Zhang, J.-R. Li, J. Li, *Chem. Eng. J.* **2018**, *346*, 489–496.
[43] H. Zeng, M. Xie, Y.-L. Huang, Y. Zhao, X.-J. Xie, J.-P. Bai, M.-Y. Wan, R. Krishna, W. Lu, D. Li, *Angew. Chem. Int. Ed.* **2019**, *58*, 8515–8519.
[44] L. Yan, H.-T. Zheng, L. Song, Z.-W. Wei, J.-J. Jiang, C.-Y. Su, *Chem. Eng. J.* **2023**, *472*, 145145.
[45] F. Zheng, R. Chen, Y. Liu, Q. Yang, Z. Zhang, Y. Yang, Q. Ren, Z. Bao, *Adv. Sci.* **2023**, *10*, 2207127.
[46] A. Hazra, D. P. van Heerden, S. Sanyal, P. Lama, C. Esterhuysen, L. J. Barbour, *Chem. Sci.* **2019**, *10*, 10018–10024.
[47] P. Vervoorts, J. Keupp, A. Schneemann, C. L. Hobday, D. Daisenberger, R. A. Fischer, R. Schmid, G. Kieslich, *Angew. Chem. Int. Ed.* **2021**, *60*, 787–793.
[48] A. Greenaway, B. Gonzalez-Santiago, P. M. Donaldson, M. D. Frogley, G. Cinque, J. Sotelo, S. Moggach, E. Shiko, S. Brandani, R. F. Howe, P. A. Wright, *Angew. Chem. Int. Ed.* **2014**, *53*, 13483–13487.
[49] H. Molavi, A. Eskandari, A. Shojaei, S. A. Mousavi, *Microporous Mesoporous Mater.* **2018**, *257*, 193–201.
[50] Z. Yan, Y. Gong, B. Chen, X. Wu, Q. liu, L. Cui, S. Xiong, S. Peng, *Sep. Purif. Technol.* **2020**, *239*, 116514.
[51] J. Hutter, M. Iannuzzi, F. Schiffmann, J. VandeVondele, *Wires Comput. Mol. Sci.* **2014**, *4*, 15–25.

Manuscript received: April 15, 2025
Revised manuscript received: June 27, 2025
Accepted manuscript online: July 02, 2025
Version of record online: ■■, ■■

Research Article

Metal–Organic Frameworks

K. Wang, Y. Jiang*, H. Zhang, S. Jia, Q. Wang, P. Cui*, T. AlShahrani, S. Ma* — **e202508419**

Engineering the Microporous Environment of Flexible Metal–Organic Frameworks with Bifunctionality for Promoting the Separation of Ethylene from a Ternary Mixture

A rationally designed flexible metal–organic framework featuring an engineered microporous environment with bifunctionality was achieved to provide high binding affinity for both CO_2 and C_2H_2 and to enable efficient one-step separation of C_2H_4 from a ternary mixture of $CO_2/C_2H_2/C_2H_4$.